Young's modulus mapping on SCS-6 SiC_f/Ti-6Al-4V composite by electromagnetic-resonance-ultrasound microscopy

Jiayong Tian,[a] Hirotsugu Ogi, Toyokazu Tada, and Masahiko Hirao
Graduate School of Engineering Science, Osaka University, Machikaneyama 1-3, Toyonaka, Osaka 560-8531, Japan

(Received 20 June 2003; accepted 15 September 2003)

Electromagnetic-resonance-ultrasound microscopy was applied to visualize Young's-modulus distribution in SCS-6 SiC fiber/Ti-6Al-4V composite. Resonance of a piezoelectric langasite ($La_3Ga_5SiO_{14}$) crystal is excited and detected by a surrounding solenoid coil without any contact between them. Point contact with the specimen causes a shift in resonance frequency of the order of 10^{-4}, depending on the local elastic stiffness of the contacting material. Two-dimensional stepping on the specimen surface provides the image of Young's-modulus distribution. Calibration measurements based on contact theory allow determination of Young's moduli of the carbon core (150 GPa), SiC sheaths (180–505 GPa), and Ti-6Al-4V matrix (90 GPa). The radial variation of Young's modulus depicts the concentric multi-phase layers in an SCS-6 fiber. © *2003 American Institute of Physics.* [DOI: 10.1063/1.1623611]

I. INTRODUCTION

SiC-fiber-reinforced titanium-alloy composites are promising materials for aeronautical components, because they show high tensile strength, low mass density, and low thermal expansion at elevated temperatures. Study of their elastic constants is of great important for designing such an application. Much research has appeared on their microstructure,[1,2] chemical composition,[1] mechanical properties,[3,4] and interfacial properties.[2] Concerning the SCS-6 SiC fiber,[5] some studied the relationship between the elasticity and microstructure. Ning and Pirouz[1] used high-resolution transmission electron microscopy (TEM) to investigate the microstructures in the carbon-core, carbon-coating, and SiC regions. They also studied the chemical-composition variation along the radial direction of the fiber. Sathish Cantrell, and Yost[6] gave the upper and lower bounds of the bulk, shear, and Young's moduli over the fiber's cross-section with the Hashin–Shtrikman formula. Mann *et al.*[7] applied the nano-identation technique to measure the hardness and Young's modulus of the SCS-6 fibers along the radial direction. They gave Young's moduli of 28 GPa for the carbon core, 21 GPa for the carbon coating, and 333 GPa for the whole fiber.

However, there are large discrepancies between Young's moduli evaluated by the nano-indentation method and those predicted from the microstructure observations. Ning and Pirouz[1] revealed that the carbon core consists of randomly oriented turbostratic-carbon (TC) blocks; the carbon coating consists of textured TC blocks, whose *c* axes are aligned in the radial direction. Using the graphite's monocrystal elastic constants, the Hill average predicts Young's modulus of the carbon core to be 260 GPa. Axial Young's modulus of the carbon coating should be much larger than this value because of the texture. Moreover, the cross-sectional average of Young's modulus by the nano-indentation method is smaller than those reported previously (400–430 GPa).[8–11]

The objective of the present study is to evaluate the local Young's modulus of the SCS-6 SiC_f/Ti-6Al-4V composite by electromagnetic-resonance-ultrasound microscopy (ERUM).[12] This detects the resonance-frequency shift of a langasite crystal caused by point contact with the specimen. The acoustic resonance is excited and detected with the piezoelectric effect using a contactless solenoid coil. To stabilize the contact/positioning and enhance the sensitivity, a biasing force is needed, which we apply to the nodal points of the probe's top face. Thus, the probe is isolated from all the mechanical contacts except for the point contact with the specimen surface. This configuration enables a stable and sensitive measurement of the resonance-frequency shift for deducing Young's modulus of the local region, where the probe tip is tapping.

II. MATERIAL

A metal-matrix composite made up of polycrystalline Ti-6Al-4V matrix and unidirectional reinforcing SCS-6 SiC fibers was studied. It was produced by a foil-fiber-foil technique (eight plies) at 900 °C with 65 MPa hydrostatic compression. Figure 1(a) shows the microstructures. The SiC fiber is 143 μm in diameter and the fiber volume fraction is 0.35. The average grain size of the matrix alloy is 9 μm.

Before the elastic-constant mapping, the cross section of the specimen was mechanically polished with finer abrasive papers and then with colloidal diamond particles (0.1 μm).

Ning and Pirouz's TEM study[1] revealed a concentrically layered structure of multiple phases in an SCS-6 fiber [Fig. 1(b)]. The fiber is fabricated by a series of chemical vapor depositions (CVDs). First, 1.5-μm-thick pyrolithic carbon is deposited on a carbon filament of 16.5 μm radius, and deposition of 50-μm-thick SiC sheath follows. Then, 3-μm-thick

[a]Author to whom correspondence should be addressed; electronic mail: J_tian@me.es.osaka-u.ac.jp

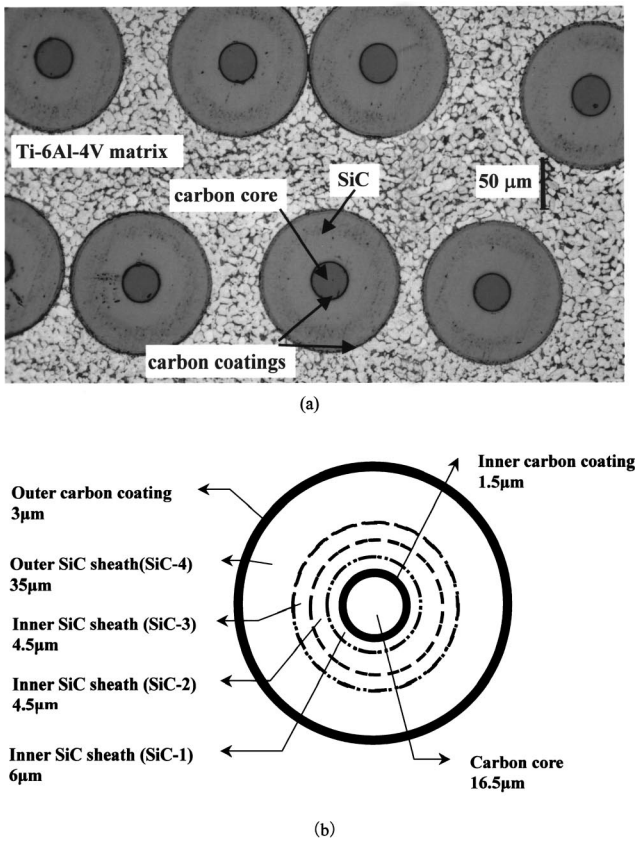

FIG. 1. (a) Mircostructure of SCS-6 SiC_f/Ti-6Al-4V composite and (b) schematic showing multilayered structure.

carbon-rich coating containing SiC particles is deposited on the SiC sheath to avoid the surface damage and increase the interfacial strength. The SiC sheath contains four layers labeled by SiC-1, SiC-2, SiC-3, and SiC-4. They have slightly different carbon content and grain orientation. SiC-1, SiC-2, and SiC-3 consist of carbon-rich β-SiC grains. The SiC-4 layer is composed of nearly stoichiometric β-SiC grains.[1]

III. ELECTROMAGNETIC-RESONANCE-ULTRASOUND MICROSCOPY

Figure 2 shows the setup of ERUM. An oriented rectangular-parallelepiped piezoelectric crystal of langasite stands in a surrounding solenoid coil. A spherical bearing of tungsten carbide (WC) is bonded at the center of the bottom surface. The probe touches the specimen, fixed on an X-Y stage, through this bearing. Stepped sweeping of the specimen provides a two-dimensional image of elastic-constant distribution.

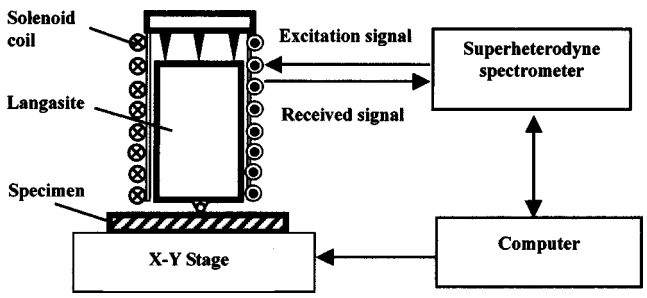

FIG. 2. Measurement setup of ERUM. The probe is an oriented rectangular-parallelepiped measuring $L_1=10.012$ mm, $L_2=10.043$ mm, and $L_3=14.405$ mm.

Langasite is a trigonal-symmetry crystal, whose elastic constants C_{ij}, piezoelectric coefficients e_{ij}, and dielectric coefficients ε_{ij} are given as[13]

$$[C_{ij}]=\begin{bmatrix} 188.5 & 104.7 & 96.87 & 14.11 & 0 & 0 \\ & 188.5 & 96.87 & -14.11 & 0 & 0 \\ & & 263.11 & 0 & 0 & 0 \\ & & & 53.35 & 0 & 0 \\ & \text{sym.} & & & 53.35 & 14.11 \\ & & & & & 41.9 \end{bmatrix} \times(\text{GPa}), \tag{1}$$

$$[e_{ij}]=\begin{bmatrix} -0.429 & 0.429 & 0 & 0.193 & 0 & 0 \\ 0 & 0 & 0 & 0 & -0.193 & 0.429 \\ 0 & 0 & 0 & 0 & 0 & 0 \end{bmatrix} \times(\text{C/m}^2) \tag{2}$$

and

$$[\varepsilon_{ij}]=\begin{bmatrix} 19.05 & 0 & 0 \\ & 19.05 & 0 \\ \text{sym.} & & 50.50 \end{bmatrix}\varepsilon_0, \tag{3}$$

where ε_0 denotes the dielectric constant in vacuum. Piezoelectric coefficients of langasite are larger than those of quartz (langasite's $|e_{11}|$ and $|e_{14}|$ are larger than those of quartz by factors 2.3 and 4.5, respectively) and an electric excitation can effectively cause oscillation to the crystal without any contact. Furthermore, the elastic constants show lower temperature derivatives, of the order of $10^{-5}\,\text{K}^{-1}$,[14] which assures the stable resonance frequencies.

The solenoid coil is driven by high-power rf bursts to generate an oscillating electromagnetic field. The electric field interacts with langasite through the converse piezoelectric effect and excites a vibration of the langasite probe.[13] After the excitation, the same coil receives the vibration of the probe by the piezoelectric effect. The received signal is fed to a superheterodyne spectrometer to extract the in-phase and out-of-phase components to calculate the amplitude from the root of the sum of their square.[15,16] A frequency scan provides a resonance spectrum as shown in Fig. 3.

In order to analyze the resonance of the crystal probe contacting the specimen, the bearing-specimen contact is approximated as a spring support with spring constant k_{ij}. The normal spring constant k_{33} and tangential spring constants k_{11} and k_{22} are assumed to be independent of each other; and $k_{ij}=0$ for $i\neq j$. For a vibrating piezoelectric elastic crystal with the spring support, Lagrangian Π is expressed as[13]

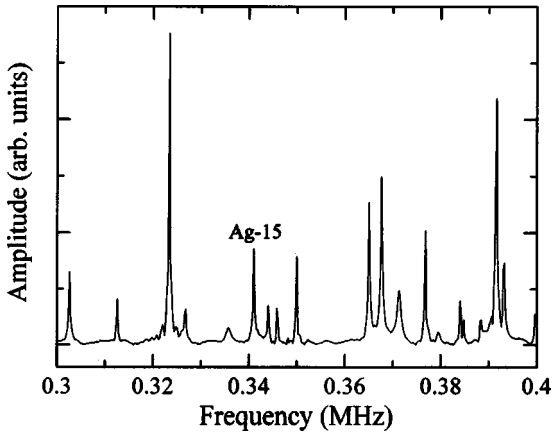

FIG. 3. Free-vibration resonance spectrum of a langasite probe measured by the contactless surrounding coil through the piezoelectric effect.

$$\Pi=\frac{1}{2}\int\int\int_{\Omega}(S_{ij}C_{ijkl}S_{kl}+2S_{ij}e_{ijk}\phi_{,k}-\phi_{,i}\varepsilon_{ij}\phi_{,j}-\rho\omega^2u_i)dV+\frac{1}{2}\int\int_{\Gamma}k_{ij}u_ju_idS, \tag{4}$$

where S_{ij}, ρ, u_i, and ϕ are the strain tensor, mass density, displacement, and electric potential, respectively. Ω and Γ denote the volume and the surface of the piezoelectric crystal, respectively. Because the exact solutions are unavailable, we express the displacement vector $\mathbf{U}=[u_1,u_2,u_3]^T$ and the electric potential ϕ in linear combinations of orthogonal basis functions $\mathbf{Y}$ as

$$\mathbf{U}=\mathbf{Ya}, \tag{5}$$

$$\boldsymbol{\phi}=\mathbf{Yb}, \tag{6}$$

where **a** and **b** are unknown coefficient vectors. Legendre polynomials P_k are selected as the orthogonal basis, which are given by

$$Y^{(p)}(x_1,x_2,x_3)=\frac{1}{\sqrt{L_1L_2L_3}}\sqrt{\frac{2k+1}{2}}\sqrt{\frac{2m+1}{2}}\times\sqrt{\frac{2n+1}{2}}P_k\left(\frac{x_1}{L_1}\right)P_m\left(\frac{x_2}{L_2}\right)P_n\left(\frac{x_3}{L_3}\right). \tag{7}$$

Here, L_i denotes the edge length of the rectangular parallelepiped along the x_i axis. Substitution of Eqs. (5)–(7) into Eq. (4) yields the resonance frequencies and corresponding displacement distributions of the probe with Lagrangian minimization ($\delta\Pi=0$).

Free vibrations of an oriented rectangular parallelepiped of langasite fall into four groups labeled by Ag, Au, Bg, and Bu.[17] We selected Ag-15 mode for the present measurement. Using Eqs. (4)–(7), we calculated the displacements with each resonance mode and found that the out-of-plane displacement (u_3) of Ag-15 mode has an antinode near the center of the bottom surface [Fig. 4(a)] and the in-plane displacements (u_1 and u_2) have nodes at this point. The numerical calculation by Eq. (4) also verify that the resonance frequency of Ag-15 then shows a sufficiently large sensitivity to the normal spring constant k_{33} and it is insensitive to the tangential constants k_{11} and k_{22}.

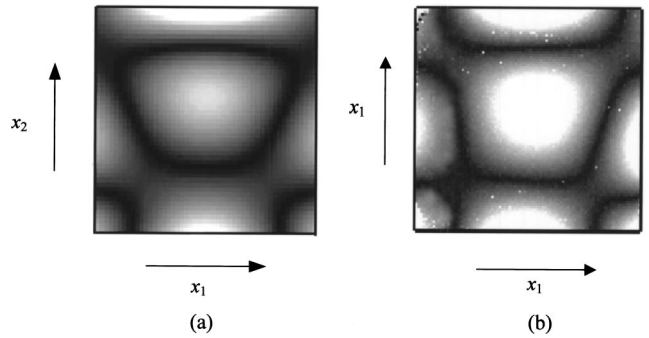

FIG. 4. Distribution of the normal displacement u_3 of Ag-15 mode at the upper surface of the probe. (a) Calculation and (b) measurement by laser-Doppler interferometry.

We identified Ag-15 mode by measuring the displacement amplitude of u_3 using laser-Doppler interferometry [see Fig. 4(b)] and comparing it with the calculation in Fig. 4(a). The calculation and measurement agree well with each other, confirming the mode identification and the location of nodes and antinodes. Because u_1 and u_2 of this mode show the nodes at the bottom center point, the tangential contact stiffness has little influence on Ag-15 mode and we ignored k_{11} and k_{22} in Eq. (4)

According to the classical contact theory,[18] the normal-contact spring stiffness k_{33} is

$$k_{33}=AE^{*\delta_3}, \tag{8}$$

where the effective Young's modulus E^* is given by

$$\frac{1}{E^*}=\frac{1-\nu_1^2}{E_1}+\frac{1-\nu_2^2}{E_2}. \tag{9}$$

E and ν are Young's modulus and Poisson's ratio; the subscripts 1 and 2 denote the bearing and the specimen, respectively. Here, constants A and δ_3 depend on the biasing force F_0 and the shape of the contacting elements. For example, $\delta_3=2/3$ and $A=\sqrt[3]{6RF_0}$ for the contact of two elastic spheres of radius R (Hertz contact). The contact is more complicated in the present case, because three elements (langasite, bearing, and specimen) participate. We assume that the dependence in the form of Eq. (8) is still valid, where A and δ_3 are determined from calibration measurements. Figure 5 shows the regression curve for the measured resonance-frequency shifts with an acrylic plate, (100) surface of monocrystal silicon, and a tungsten–carbide plate. We used a tungsten–carbide sphere bearing of 0.35 mm radius and the biasing force of $F_0=0.41$ N. The free-vibration resonance frequency was $f_0=0.342\,877$ MHz.

IV. RESULTS AND DISCUSSION

Figure 6(a) presents an ERUM image of the composite. The probe scanned the surface at every 5 μm. Figure 6(b) shows the result of a linear scanning along the dashed line in Fig. 6(a). Young's modulus in the SiC-fiber region varies in

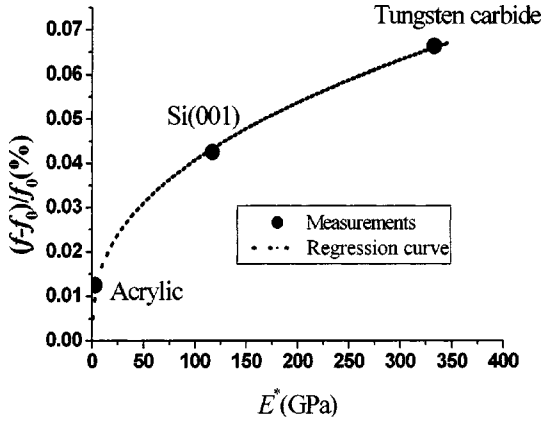

FIG. 5. Resonance-frequency shifts by touching three reference materials, and the regression curve based on the contact theory. E^* denotes the effective Young's modulus of the material and f_0 the free-vibration resonant frequency of the langasite probe.

an axisymmetric way. This demonstrates that microstructure of the SiC fiber is strongly dependent on the CVD condition. Assuming Poisson's ratio to be 0.25, Young's moduli were inversely calculated to be 150±78 GPa for the carbon core, 180–400 GPa for the SiC inner sheaths (SiC-1–3), 505±115 GPa for the SiC outer sheath (SiC-4), and 90±20 GPa for the matrix. Our result of carbon core is several times larger than the previous measurements (28 GPa in Ref. 7 and 40 GPa in Ref. 19). The Hertz-contact theory predicts the contact radius to be larger than 6 μm, while the TC blocks were measured to be 1–50 nm in diameter. Thus, one measurement includes many TC grains and the ERUM provides the orientation-averaged Young's modulus for the carbon core. As mentioned above, the Hill-average Young's modulus is 260 GPa in the carbon core, which is closer to our result, but still larger. We attribute this to incohesive bonding or microcracking at the TC-block boundaries.

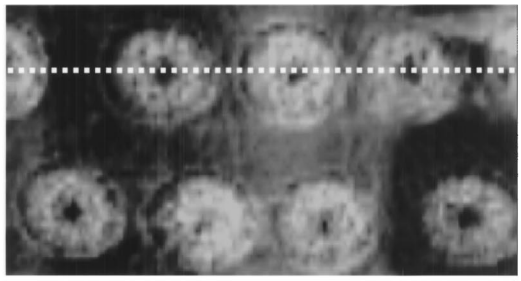

(a)

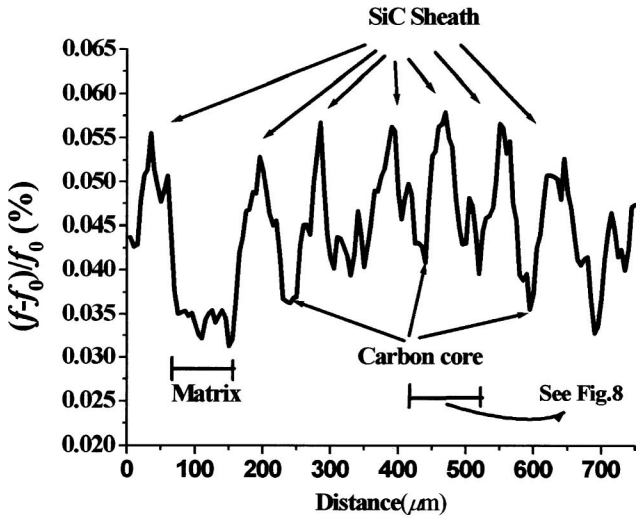

(b)

FIG. 6. The ERUM image of the composite measured with the 0.35 mm radius bearing and 0.41 N biasing force. (a) Two-dimensional image and (b) line trace of the frequency shift shown in (a).

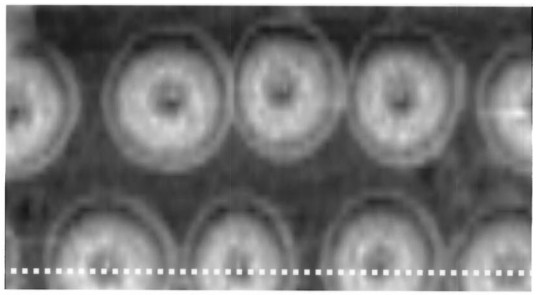

(a)

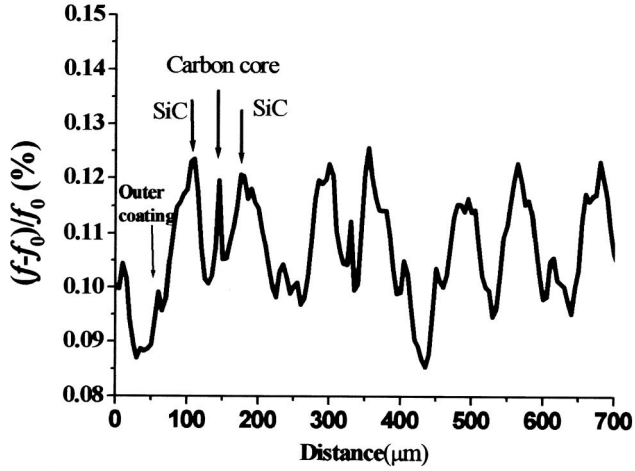

(b)

FIG. 7. The ERUM image of the composite measured with the 0.5 mm radius bearing and 0.73 N biasing force. (a) Two-dimensional image and (b) line trace of the frequency shift shown in (a).

Young's modulus of (isotropic) polycrystalline Ti-6Al-4V was reported to be 111 GPa,[20] which agrees with our measurement. Note that the tip-contact area is comparable with the grain size (~9 μm) and the modulus in the matrix region will vary at every measuring point depending on the crystallographic orientation.

In order to study the influence of the tip radius (R) and the biasing force (F_0) on the measurements, another ERUM image of Fig. 7 was obtained using $R=0.5$ mm and $F_0=0.73$ N. The resonance-frequency shift doubles being compared with Fig. 6; the increase in R and F_0 increases the

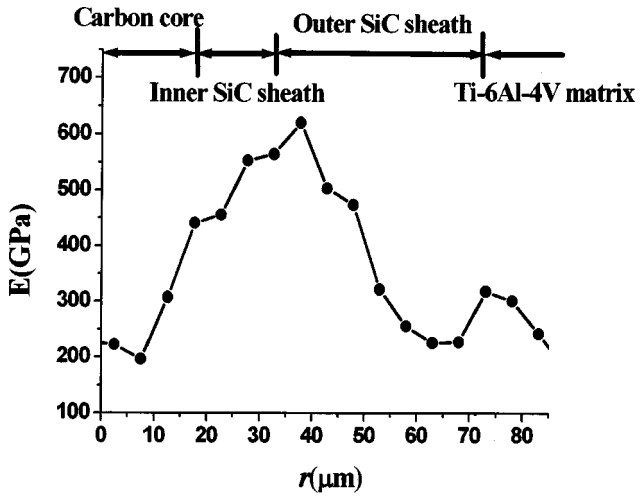

FIG. 8. Radial variation of Young's modulus across the SCS-6 SiC fiber.

sensitivity to the specimen modulus. Young's modulus of the carbon core was evaluated to be larger when using larger R and F_0. We attribute this to the larger contact area, which is estimated to be 14 μm in radius. The contact then encompasses the carbon core and the inner-carbon coating. The inner-carbon coating, consisting of the textured TC blocks, has a large Young's modulus and it increases the apparent resonance frequency when involved in the contact area. The ERUM measurement with larger tip and biasing force exhibits better modulus resolution but poorer spatial resolution.

Figure 8 shows the radial variation of Young's modulus of a single fiber measured with the finer special-resolution setup ($R=0.35$ mm and $F_0=0.41$ N). Young's modulus for the carbon core remains unchanged from $r=0$ to 10 μm, but it increases approaching $r=15\,\mu$m, where the inner carbon coating is deposited. At this point, the tip is touching the carbon core, the inner-coating layer, and the inner SiC sheath. The involvement of inner-coating layer of large Young's modulus results in the increase of the measured modulus. Note that the contacting radius is larger than 6 μm.

Young's modulus in the SiC region first increases and then decreases as the contact point moves toward the matrix. The maximum modulus occurs near the SiC-3/SiC-4 boundary ($r\approx 38\,\mu$m). This pattern is basically the same as the result in Ref. 6. The ERUM imaging detects the decreasing modulus in the outer SiC region, which is absent in the previous studies,[6,7] which gave the constant modulus throughout this region. We interpret that carbon atoms diffuse into in the outer SiC region, form nonstoichiometric SiC, and decrease the SiC modulus; ERUM with high sensitivity can sense the reduced modulus in this region. At the outer carbon coating, measured Young's modulus is relatively high, which is acceptable because it consists of the TC blocks with the basal planes parallel to the fiber radius.

V. CONCLUSION

Electromagnetic-resonance-ultrasound microscopy (ERUM) visualized local Young's modulus in an SCS-6 SiC_f/Ti-6Al-4V metal-matrix composite. We determined the modulus distribution across the SiC fiber imbedded in the Ti-alloy matrix by measuring the resonance-frequency shift of Ag-15 mode of the langasite probe and using the regression curve based on the contact theory. Obtained Young's moduli were 150 ± 78 GPa for carbon core, 180–400 GPa for SiC inner sheaths, 505 ± 115 GPa for SiC outer sheath, and 90 ± 20 GPa for matrix.

The ERUM result for the carbon core is much closer to the Hill-average prediction than those reported previously. With the better modulus resolution, ERUM is capable of characterizing fine structures, which conventional methods have not observed. This includes the radial variation in the SiC region. In the outer region, the modulus is decreased with the carbon diffusion from the outer coating. ERUM also detects the modulus increase at the outer carbon coating.

ACKNOWLEDGMENT

The first author (J. T.) acknowledges the support provided by the Japan Society for the Promotion of Science (JSPS).

[1] X. J. Ning and P. Pirouz, J. Mater. Res. **6**, 2234 (1991).
[2] M. Singh, R. Dickerson, F. Olmsted, and J. Eldridge, J. Mater. Res. **12**, 706 (1997).
[3] R. Bhatt and D. Hull, J. Am. Ceram. Soc. **81**, 957 (1998).
[4] J. Hann, G. Swift, E. Uestuenday, I. Begerlein, J. Almer, U. Lienert, and D. Haeffer, Metall. Mater. Trans. A **33A**, 3839 (2002).
[5] Textron Specialty Materials, Textron Co., Lowell, MA.
[6] S. Sathish, J. Cantrell, and W. Yost, J. Mater. Res. **9**, 2298 (1994).
[7] A. Mann, M. Balooch, J. Kinney, and T. Weihs, J. Am. Ceram. Soc. **82**, 111 (1999).
[8] M. Mittnick, *Metal Matrix Composites*, edited by G. Dvorak and C. Zweben (Technomic, Lancaster, PA, 1987).
[9] S. Mital, C. Chamis, and P. Gotsis, Comput. Sci. Technol. **50**, 59 (1994).
[10] S. Jansson, H. Deve, and A. Evans, Metall. Trans. A **22A**, 2975 (1991).
[11] H. Ogi, S. Kai, T. Ichitsubo, M. Hirao, and K. Takashima, Philos. Mag. A **83**, 503 (2003).
[12] H. Ogi, J. Tian, T. Tada, and M. Hirao, Appl. Phys. Lett. **83**, 464 (2003).
[13] H. Ogi, N. Nakamura, K. Sato, M. Hirao, and S. Uda, IEEE Trans. Ultrason. Ferroelectr. Freq. Control **50**, 553 (2003).
[14] A. Bungo, C. Jian, K. Yamaguchi, Y. Sawada, S. Uda, and Y. Pisarevsky, Jpn. J. Appl. Phys., Part 1 **87**, 7491 (2000).
[15] H. Ogi, P. Heyliger, H. Ledbetter, and S. Kim, J. Acoust. Soc. Am. **108**, 2829 (2000).
[16] M. Hirao and H. Ogi, *EMATs for Science and Industry: Noncontacting Ultrasonic Measurements* (Kluwer, Boston, 2003).
[17] I. Ohno, Phys. Chem. Miner. **17**, 371 (1990).
[18] K. L. Johnson, *Contact Mechanics* (Cambridge University Press, Cambridge, 1985).
[19] S. Sathish, J. Cantrell, and W. Yost, J. Am. Ceram. Soc. **79**, 209 (1996).
[20] E. R. Naimon, W. F. Weston, and H. Ledbetter, Cryogenics **14**, 246 (1974).